



3D carbon quantum dots/graphene aerogel as a metal-free catalyst for enhanced photosensitization efficiency

Ru Wang^a, Kang-Qiang Lu^{a,b}, Fan Zhang^a, Zi-Rong Tang^{a,*}, Yi-Jun Xu^{a,b,*}

^a College of Chemistry, New Campus, Fuzhou University, Fuzhou, 350116, PR China

^b State Key Laboratory of Photocatalysis on Energy and Environment, College of Chemistry, Fuzhou University, Fuzhou, 350116, PR China



ARTICLE INFO

Keywords:

Metal-free photocatalyst

Carbon quantum dots

Graphene aerogel

Photosensitization efficiency

Regenerability

ABSTRACT

Carbon quantum dots (CQDs) have recently emerged as the light-harvesting antennas for photocatalytic applications due to their outstanding optical absorption, nontoxicity, unsophisticated synthesis and scalable production. However, the poor photocatalytic efficiency and difficult recovery of CQDs restrict their large-scale practical applications in aqueous photocatalytic reactions. Here we report a facile synthesis of metal-free three-dimensional (3D) construction of CQDs spatially distributed into the frameworks of graphene aerogel (CQDs/GA) with enhanced photocatalytic performance compared to the bare CQDs. The photoelectrochemical characterizations demonstrate that 3D graphene aerogel (GA) with interconnected networks exhibits efficient spatial separation and transportation of photoexcited charge carriers, thereby leading to the improved photocatalytic activity of the CQDs/GA composites. In addition, such 3D bulk aerogel displays easy separability from liquid-phase reaction system and regenerability *via* simple replenishment of CQDs, which ensures the sustainable photoactivity of the CQDs/GA composites. This approach for preparing 3D CQDs/GA composites is expected to open a new vista for constructing metal-free and regenerable photocatalysts with enhanced photosensitization efficiency of CQDs.

1. Introduction

Carbon quantum dots (CQDs) have recently been regarded as a promising light absorber for solar energy conversion in virtue of their prominent ultraviolet-visible (UV-vis) light absorption [1–3]. Additionally, CQDs can be easily and massively synthesized from plentiful precursors, rendering them as substitutes of other established photosensitizers for photocatalytic applications [4–7]. Despite considerable research in this aspect, the low photosensitization efficiency of CQDs becomes a current bottleneck for their large-scale practical applications in photocatalysis. Furthermore, it is worth noting that another limitation of utilizing water-soluble CQDs in photocatalytic processes is that CQDs cannot be conveniently separated and recycled from liquid-phase reaction system. Therefore, it is highly desirable to develop CQD-based photocatalyst with enhanced photosensitization efficiency and good recyclability, which represents a key process in improving the performance of these systems.

Three-dimensional (3D) graphene aerogel (GA) has aroused wide interest recently in the field of photocatalysis [8–13]. 3D GA can provide multidimensional electron transport pathways. Namely, it not only preserves the benign electronic conductivity of two-dimensional (2D)

graphene nanosheets, but also possesses unique electron transport pathways of 3D interconnected networks [14]. Meanwhile, the hierarchical frameworks of 3D GA make it an ideal scaffold to inhibit the aggregation or stacking of subunits, thus exposing more active sites for photocatalytic reaction [15]. In addition, 3D GA can be easily recycled from liquid-phase reaction systems due to their macroscopic bulk appearance. In addition, the shapes, volumes and densities of 3D GA can be easily modulated by tuning the features of reaction vessel, which indicates the flexible possibility and feasibility of large-scale production [16].

Herein, we report 3D carbon quantum dots/graphene aerogel (CQDs/GA) composites *via* a facile hydrothermal method, which can efficiently improve the photosensitization efficiency of CQDs. The spatial networks of 3D GA can provide an ideal support for the deposition of ultrasmall nanoparticles, which renders a viable strategy for fixing the water-soluble CQDs to form recyclable 3D CQDs/GA bulk photocatalysts. The optimal photocatalytic activity of the CQDs/GA composites has been demonstrated to be 2.59 times as high as that of the blank CQDs, which can be attributed to the multidimensional electron transport pathways of their hierarchical frameworks. Furthermore, the robust and macroscopic 3D CQDs/GA can be easily

* Corresponding authors at: College of Chemistry, New Campus, Fuzhou University, Fuzhou, 350116, PR China.

E-mail addresses: zrtang@fzu.edu.cn (Z.-R. Tang), yjxu@fzu.edu.cn (Y.-J. Xu).

separated and recycled from the aqueous reaction medium with negligible mass loss. In particular, they can be regenerated via a simple re-treatment by replenishing fresh CQDs, which thus further enables the long-term photoactivity of the composite aerogel. We anticipate that this work could open a promising vista to design metal-free and regenerable photocatalysts for solar energy conversion, and as well provide a strategy for improving the photosensitization efficiency of CQDs.

2. Experimental section

2.1. Materials

Citric acid, sodium hydroxide (NaOH), hydrochloric acid (HCl), concentrated sulfuric acid (H_2SO_4 , 98%), potassium permanganate ($KMnO_4$), hydrogen peroxide (H_2O_2 , 30%), absolute ethanol (C_2H_5OH), triethanolamine (TEOA), and potassium persulfate ($K_2S_2O_8$) were all obtained from Sinopharm Chemical Reagent Co., Ltd. (Shanghai, China). The graphite powder was supplied from Qingdao Zhongtian Company, China. The deionized (DI) water used in the experiment was from local sources.

2.2. Preparation of carbon quantum dots (CQDs)

Carbon quantum dots (CQDs) were prepared by a modified literature procedure [17]. Citric acid (40 g) was thermolyzed in furnace under air at 180 °C for 40 h. Then the brown high-viscosity liquid of carboxylic acid capped CQDs was stirred with DI water (100 mL) and NaOH solution (5 M, 50 mL) to dissolve. More NaOH solution (5 M, approximately 25 mL) was subsequently added to neutralize the acidic CQDs to pH 7 resulting in an orange-brown solution of sodium carboxylate capped CQDs. Finally, the product was isolated as brown powder by freeze-drying.

2.3. Preparation of graphene oxide (GO)

Graphene oxide (GO) was prepared from natural graphite powder by a modified Hummers method [18,19]. The details were presented in the Supporting Information.

2.4. Preparation of 3D carbon quantum dots/graphene aerogel (CQDs/GA) composites

The preparation of 3D carbon quantum dots/graphene aerogel (CQDs/GA) composites was based on a very facile one-step hydrothermal method. In brief, CQDs were first dissolved in DI water to produce aqueous solutions with the concentration of 3 mg mL⁻¹. Then 0.5, 1, 1.5, or 2 mL of the prepared CQD aqueous solution were added into 6 mL of 5 mg mL⁻¹ GO solution to obtain CQDs/GO mixtures. DI water was added into the above mixtures to a volume of 12 mL. After being stirred for 1 h, the mixture was transferred into a 50 mL Teflon-lined autoclave and subjected to hydrothermal treatment at 180 °C for 12 h. The as-prepared CQDs/graphene hydrogel (CQDs/GH) was taken out with tweezers, washed several times with deionized water, and treated by freeze-drying. After that, CQDs/GA composites were obtained. The samples with different loadings of CQDs were labeled as CQDs/GA-5, CQDs/GA-10, CQDs/GA-15 and CQDs/GA-20, respectively. The blank GA was synthesized via the same procedure without the addition of CQDs.

2.5. Characterization

The morphology of the samples was determined by field emission scanning electron microscopy (FESEM) on a Hitachi New Generation cold field emission SEM SU-8000 spectrophotometer. Transmission electron microscopy (TEM) and high-resolution transmission electron microscopy (HRTEM) images were collected using a JEOL Model JEM

2010 EX microscope at an accelerating voltage of 200 kV. A Nanoscope IIIA system was used to measure the atomic force microscopy (AFM) spectra. Samples were dispersed on mica plate for the test. Nitrogen adsorption–desorption isotherm and the Brunauer–Emmett–Teller (BET) surface areas were collected at 77 K using Micromeritics ASAP2020 equipment. The crystal phase properties of the samples were analyzed with a powder X-ray diffractometer (Bruker D8 Advance) using Ni-filtered Cu $K\alpha$ radiation ($\lambda = 1.5418 \text{ \AA}$) in the 2θ range from 5° to 80° with a scan rate of 0.02° per second. X-ray photoelectron spectroscopy (XPS) was performed on a Thermo Scientific ESCA Lab 250 spectrometer, which was made of a monochromatic Al $K\alpha$ as the X-ray source, a hemispherical analyzer, and a sample stage with multi-axial adjustability to obtain the surface composition of the samples. All of the binding energies were calibrated by the C1s peak at 284.6 eV. Fourier-transform infrared spectroscopy (FTIR) was carried out on a Nicolet Nexus 670 FTIR spectrometer with a DTGS detector. The photoluminescence (PL) emission spectra of CQDs aqueous solution were investigated on Hitachi F4600 spectrophotometer with different excitation wavelength. The ultraviolet-visible (UV-vis) spectrum of CQDs aqueous solution was analyzed on a UV-vis spectrophotometer (UV-1750, Shimadzu Co.). UV-vis diffuse reflectance spectra (DRS) were recorded on a Cary-500 UV-vis-NIR spectrometer in which BaSO₄ powder was used as the internal standard to obtain the optical properties of the samples over a wavelength range of 200–800 nm. The photocurrent measurements were performed in a three-electrode quartz cell with an electrochemical workstation (Autolab, PGSTAT204). A Pt plate was used as the counter electrode, and an Ag/AgCl electrode was used as the reference electrode. The working electrode was prepared on fluorine-doped tin oxide (FTO) glass that was cleaned by ultrasonication in ethanol for 30 min and dried at 60 °C. Typically, 5 mg of the sample powder was ultrasonicated in 0.5 mL of *N*, *N*-dimethylformamide (DMF) to disperse it evenly to get slurry. The slurry was spread onto FTO glass, whose side part was previously protected using Scotch tape. After air-drying, the working electrode was further dried at 100 °C for 2 h to improve adhesion. Then the Scotch tape was unstuck, and the uncoated part of the electrode was isolated with epoxy resin. The exposed area of the working electrode was 0.283 cm². The electrolyte was 0.2 M aqueous Na₂SO₄ solution (pH = 6.8) without additive. Electrochemical impedance spectroscopy (EIS) measurement was carried out in the presence of 0.5 M KCl solution containing 0.01 mM K₃[Fe(CN)₆]₁/K₄[Fe(CN)₆]₁ (1:1) by applying an AC voltage with 5 mV amplitude in a frequency range from 1 Hz to 85 kHz with the open circuit potential conditions.

2.6. Photocatalytic performance

The photocatalytic reduction of Cr (VI) over the as-synthesized samples was performed in an aqueous solution under the UV-vis light irradiation. A CQDs/GA sample 60 μL of triethanolamine (TEOA, sacrificial agent) were added into 40 mL of 10 mg L⁻¹ aqueous solution of Cr (VI) in a quartz vial. The pH value of this system was about 8.5. Before UV-vis light illumination, the above suspension was kept in the dark for 2 h to establish adsorption–desorption equilibrium between the photocatalysts and the reactants. A 300 W commercial Xe lamp (PLS-SXE300/300UV, Beijing Perfectlight Co., Ltd.), emitting UV-vis light (200 nm ≤ λ ≤ 780 nm) with an energy output of 0.7 W cm⁻² was placed at a distance of approximate 10 cm from the reactor. During the reaction process, 2 mL of sample solution was collected at a certain time interval and analyzed on a UV-vis spectrophotometer (UV-1750, Shimadzu Co.). The whole experimental process was conducted under N₂ bubbling at a flow rate of 60 mL min⁻¹. The percentage of reduction of Cr (VI) was reported as C/C₀. Here, C was the concentration of Cr (VI) solution at each irradiated time interval, while C₀ was the initial concentration of Cr (VI) before the UV-vis light irradiation.

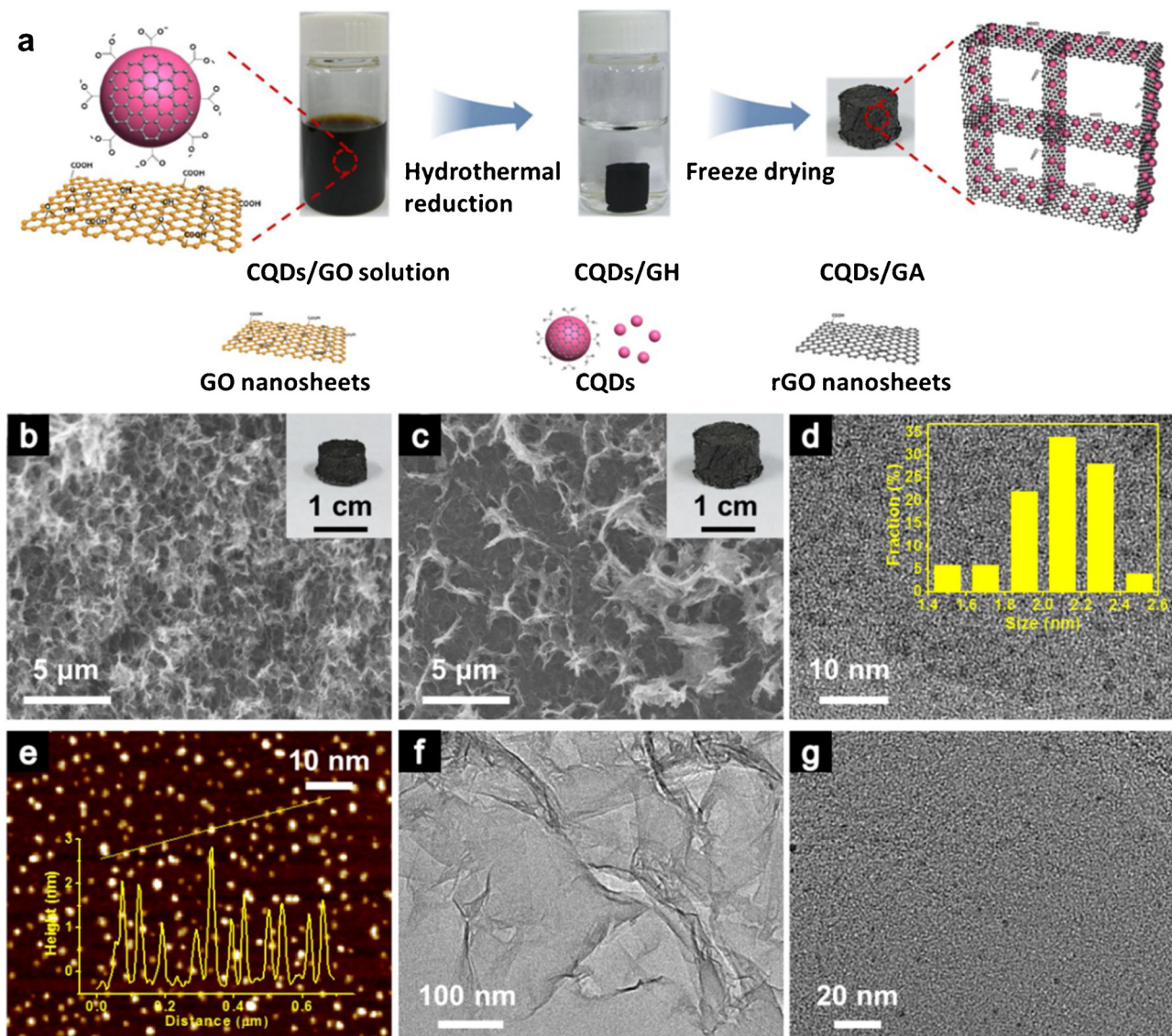


Fig. 1. (a) Synthesis procedure of the 3D CQDs/GA composite. (b, c) Scanning electron microscopy (SEM) images of the blank GA and the CQDs/GA-15, respectively. Insets in b and c: photographs of the blank GA and the CQDs/GA-15, respectively. (d) Transmission electron microscopy (TEM) image of CQDs, inset: particle-size distribution histogram of CQDs. (e) Atomic force microscopy (AFM) image of CQDs, inset: the section analysis CQDs. (f, g) TEM and high-resolution transmission electron microscopy (HRTEM) images of the CQDs/GA-15.

2.7. Recycling test and regeneration of the CQDs/GA composites

The recycling test of the synthesized aerogel catalyst was done as follows. Typically, when a photocatalytic cycle was finished, the aerogel catalyst was separated from the reaction solution using tweezers, rinsed, and then directly employed in the next photocatalytic cycle. Between the two cycles, it was unnecessary to perform tedious centrifugation, sonication, and drying processes. We regenerated the CQDs/GA composites via a very simple rehydrothermal treatment of the used CQDs/GA photocatalysts with fresh CQDs. In details, fresh CQDs were first dissolved in DI water to produce aqueous solution. Then the aqueous solution of fresh CQDs and the used CQDs/GA photocatalysts were added into a 50 mL Teflon-lined autoclave and subjected to hydrothermal treatment at 180 °C for 12 h.

3. Results and discussion

Fig. 1a illustrates the synthesis procedure of the 3D CQDs/GA composite. Before the hydrothermal reaction, CQDs are dispersed sufficiently in graphene oxide (GO) aqueous solution, in which the CQDs

could be adsorbed effectively on the surface of GO due to the π - π interactions between them [20]. Then the subsequent hydrothermal reduction causes significant removal of the hydrophilic oxygen-containing functional groups of GO nanosheets. The transformation of GO to reduced GO (rGO) nanosheets leads to the recovery of π - π conjugation between rGO layers [21]. Simultaneously, the residual hydrophilic regions of rGO nanosheets can absorb water through hydrogen bonding, which hinder the parallel stacking of the sheets, resulting in the formation of the 3D structure [22]. Finally, the 3D CQDs/graphene hydrogel (CQDs/GH) is dehydrated by the freeze-drying process to form the 3D CQDs/GA composites. The CQDs/GA-15 cylinder is about 1 cm in height and 1.2 cm in diameter, appearing larger than the blank GA as displayed in the insets of Fig. 1b and c. Furthermore, the microstructure of the CQDs/GA-15 composite and the blank GA was characterized by scanning electron microscopy (SEM) as shown in Fig. 1b and c, indicating that the CQDs/GA-15 composite possesses larger spatial networks than the blank GA does. Simultaneously, it has been observed that the samples with different loadings of CQDs possess enlarged macroscopic appearance and spatial network with the increase of CQDs content, as shown in Fig. S2. This could be

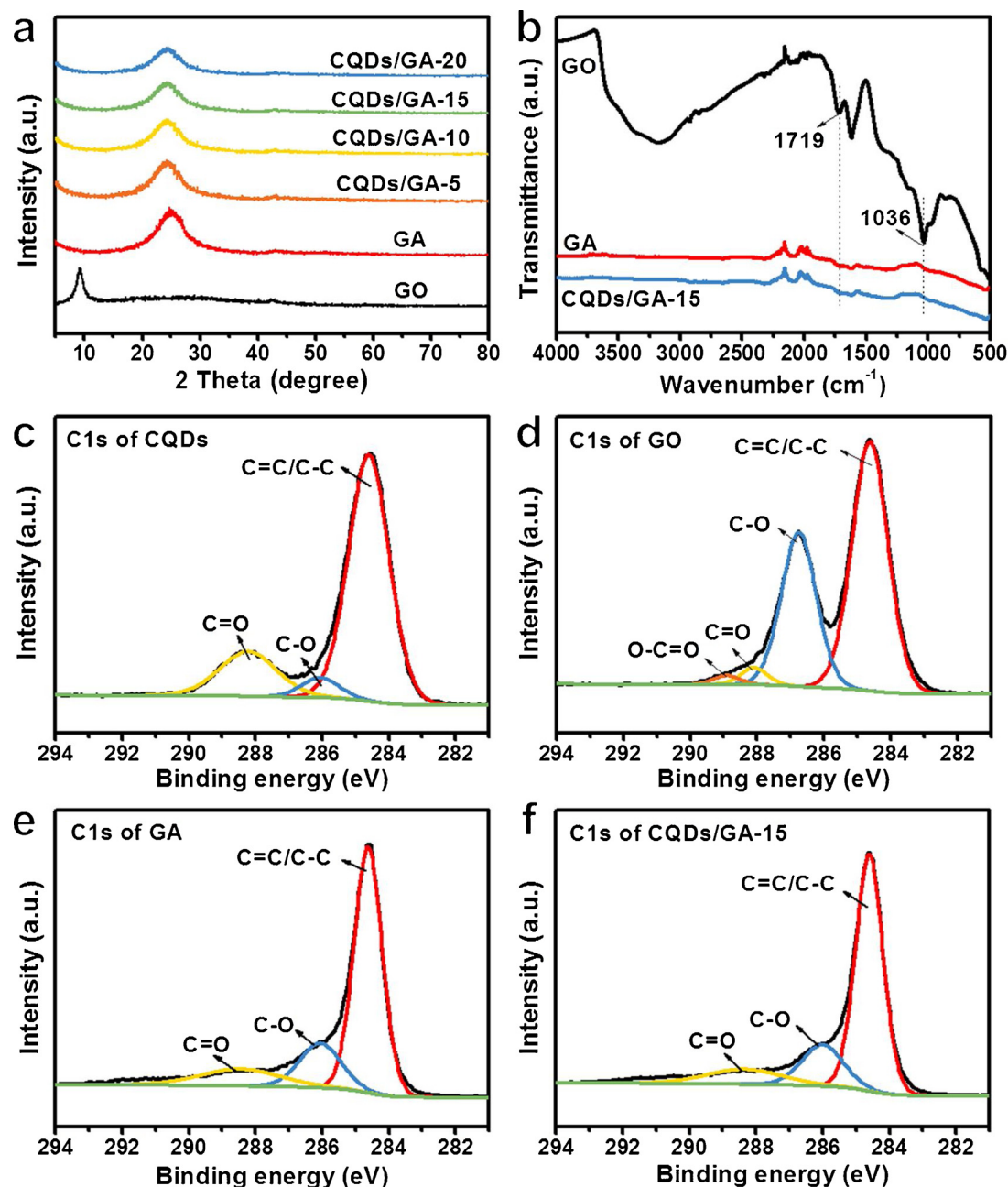


Fig. 2. (a) Powder X-ray diffraction (XRD) patterns of GO, GA and the series of CQDs/GA samples. (b) Fourier-transform infrared spectroscopy (FTIR) of GO, GA and CQDs/GA-15. (c-f) X-ray photoelectron spectroscopy (XPS) of C1s of CQDs, GO, GA and CQDs/GA-15, respectively.

attributed to the increased encapsulation of water by surface oxygenated groups of CQDs [23,24] during the hydrothermal process. However, it is noticeable that when more CQDs (e.g., 25%) are injected to the GO solution during the synthesis process, the obtained CQDs/GA composite becomes soft and fragile, as shown in Fig. S3. This could be ascribed to the high content of CQDs leading to the large coverage of the GO surface with CQDs, which reduces the number of cross-linking sites among graphene nanosheets and suppresses the formation of interconnected networks of 3D hydrogel. Therefore, considering the mechanical strength of the CQDs/GA composites, the largest mass ratio of CQDs and GA has been determined to be 20%.

The morphology and structure properties of the CQDs/GA composites and the blank CQDs were further examined by transmission electron microscopy (TEM) and atomic force microscopy (AFM). The TEM image (Fig. 1d) of CQDs indicates that the particle size mainly ranges from 1.9 to 2.2 nm with an average size of 2 nm. Fig. 1e reveals the 2D

AFM image of CQDs. The AFM line-scan profile inset in Fig. 1e shows the topographic height of CQDs, which mostly ranges from 1.5 to 2 nm with an average height of 1.8 nm. These results manifest that the as-prepared CQDs are quasi-spherical in shape and ultrasmall in size. The high-resolution transmission electron microscopy (HRTEM) image of CQDs shows the lattice fringes of 0.25 nm (Fig. S4), corresponding to the (100) facet of graphite [25]. Fig. 1f shows the TEM image of the CQDs/GA-15 composite, manifesting that its 3D interconnected framework is composed of graphene nanosheet building blocks. The HRTEM image of the CQDs/GA-15 confirms the uniform distribution of CQDs onto the surface of GA, as shown in Fig. 1g. In addition, the surface area and pore structure of the CQDs/GA composites were investigated. Fig. S5a displays the nitrogen adsorption–desorption isotherm of the CQDs/GA-15, which exhibits characteristic type IV property with a typical hysteresis loop of mesopores [26]. And the prompt increase of the adsorption at relatively high pressure ($P/P_0 = 0.8\text{--}1.0$)

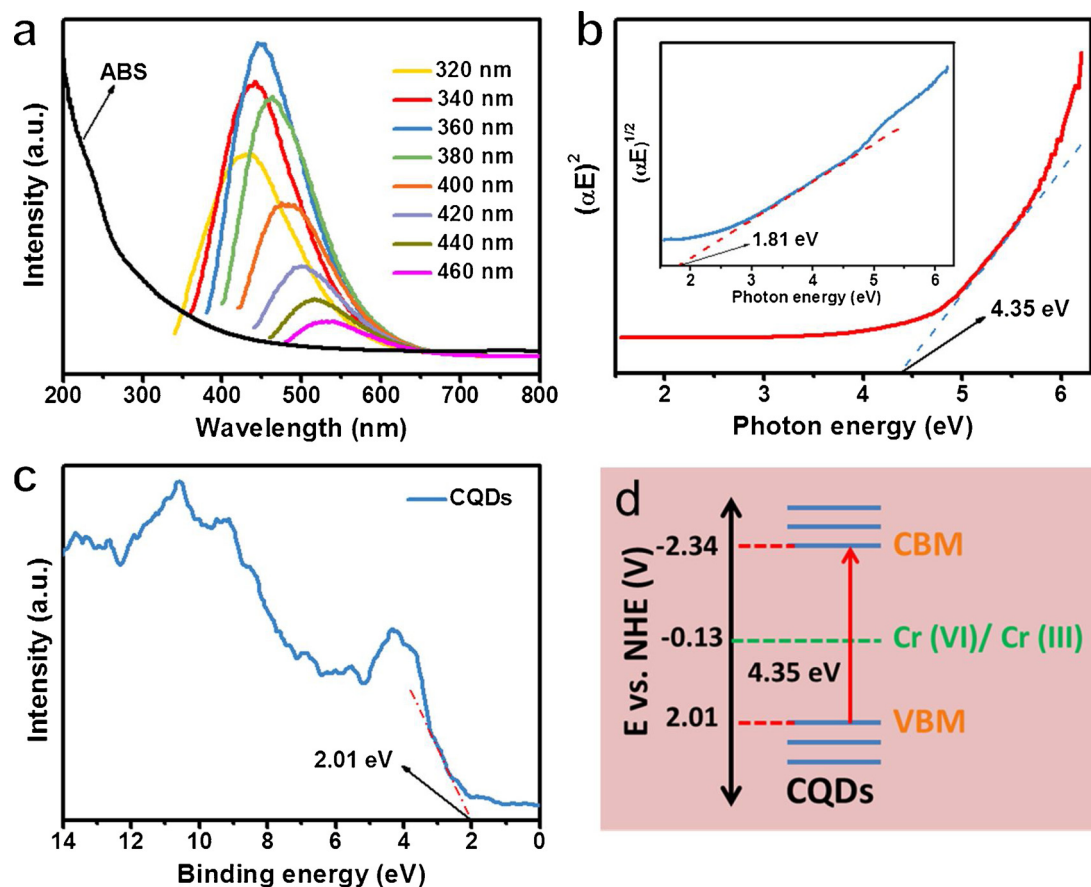


Fig. 3. (a) UV-vis absorption (ABS) spectrum and photoluminescence (PL) emission spectra of a solution of CQDs (0.1 mg mL^{-1}). (b) Plots of $(\alpha E)^2$ against photon energy (E) for the CQDs. Inset shows plots of $(\alpha E)^{1/2}$ against photon energy (E) for the CQDs. (c) Valence-band XPS spectrum for the CQDs. (d) Band structure diagram for the CQDs.

reveals the feature of macropores [27], which is further confirmed by the corresponding pore diameter distribution curve (Fig. S5b). The Brunauer–Emmett–Teller (BET) specific surface area of the CQDs/GA-15 is measured to be $151.82 \text{ m}^2 \text{ g}^{-1}$, while its adsorption cumulative pore volume is $0.56 \text{ cm}^3 \text{ g}^{-1}$.

Powder X-ray diffraction (XRD) patterns were performed to characterize the phase and graphitic structure of the as-prepared CQDs/GA samples, blank CQDs, GO and GA. As shown in Fig. S7, the XRD spectrum of the bare CQDs displays a broad peak at 25.1° , which corresponds to the (200) reflection of disordered graphitic-like species [28]. The low signal-to-noise ratio indicates the sample is partly amorphous, which can be ascribed to the surface oxygenated groups of CQDs [29]. As exhibited in Fig. 2a, GO features peak at 9.4° corresponding to the (001) diffraction. The calculated interlayer space of GO (0.87 nm) is much larger than that of graphite (0.34 nm), due to the abundant oxygen content of GO [30]. After the hydrothermal process, the peaks at 9.4° almost disappears and the broad peaks around 24.5° are observed in the GA and the CQDs/GA composites, which correspond to the (002) diffraction and indicate the effective reduction of GO [21]. Furthermore, we can see that the CQDs/GA composites possess the decreased diffraction intensity with the increased loading of CQDs.

Fourier-transform infrared spectroscopy (FTIR) was conducted to determine the functional groups of the samples of CQDs, GO, GA and CQDs/GA-15. As shown in Fig. S8, CQDs possess strong features at wavenumber of 1390 , 1559 and 1698 cm^{-1} , corresponding to the symmetric and antisymmetric stretches of the carboxylate groups, and the carbonyl moieties, respectively [17]. As shown in Fig. 2b, the FTIR spectra of GO, GA and CQDs/GA-15 support the existence of oxygenated functional groups by showing C=O (1719 cm^{-1}) peak and C-O

(1036 cm^{-1}) peak. Additionally, the peak intensity of C-O and C=O decreases remarkably in the spectra of GA and CQDs/GA-15 in comparison with that of GO due to the reduction of GO into rGO [12]. X-ray photoelectron spectroscopy (XPS) was employed to obtain more detailed information on oxygenated functional groups in the as-prepared samples. The C1s spectra can be well fitted to C=C/C-C (284.6 eV), C-O (286.2 eV) and C=O (288.4 eV) as displayed in Fig. 2c-f [31]. CQDs display an obvious C=O peak (Fig. 2c), which is consistent with the results of FTIR. For GO (Fig. 2d), a large amount of C-O detected indicates its highly oxidized state of surface. As shown in Fig. 2e, GA shows noticeable decrease in C-O peak compared with GO, revealing the efficient reduction of GO. Compared with the bare GA, the CQDs/GA-15 displays no obvious change of intensity for C-O peak and C=O peak (Fig. 2f), which could be attributed to the low content of CQDs.

The optical properties of the CQDs were investigated by UV-vis absorption spectrum and photoluminescence (PL) spectroscopy, as shown in Fig. 3a. The solution of CQDs (0.1 mg mL^{-1}) presents a broad absorption in the UV region with a tail in the near-visible region, which corresponds to various $\pi-\pi^*$ (C=C) and $n-\pi^*$ (C=O) transitions, respectively [32]. As shown in the PL emission profile, CQDs display typical excitation-wavelength dependent behavior using varying excitation wavelengths from 320 to 480 nm . The above optical properties imply that CQDs can act as a promising UV-vis light photosensitizer. To further determine the energies for the direct and indirect gap transitions of CQDs, we plotted the square and square root of the absorption energy (αE , where α is the absorbance) against the photon energy (E) [33]. It is clearly seen that the energy gap (E_g) value of CQDs is 4.35 eV for direct transition, whereas the E_g value of CQDs is 1.81 eV for indirect transition (Fig. 3b). At the same time, ultraviolet photoelectron spectroscopy

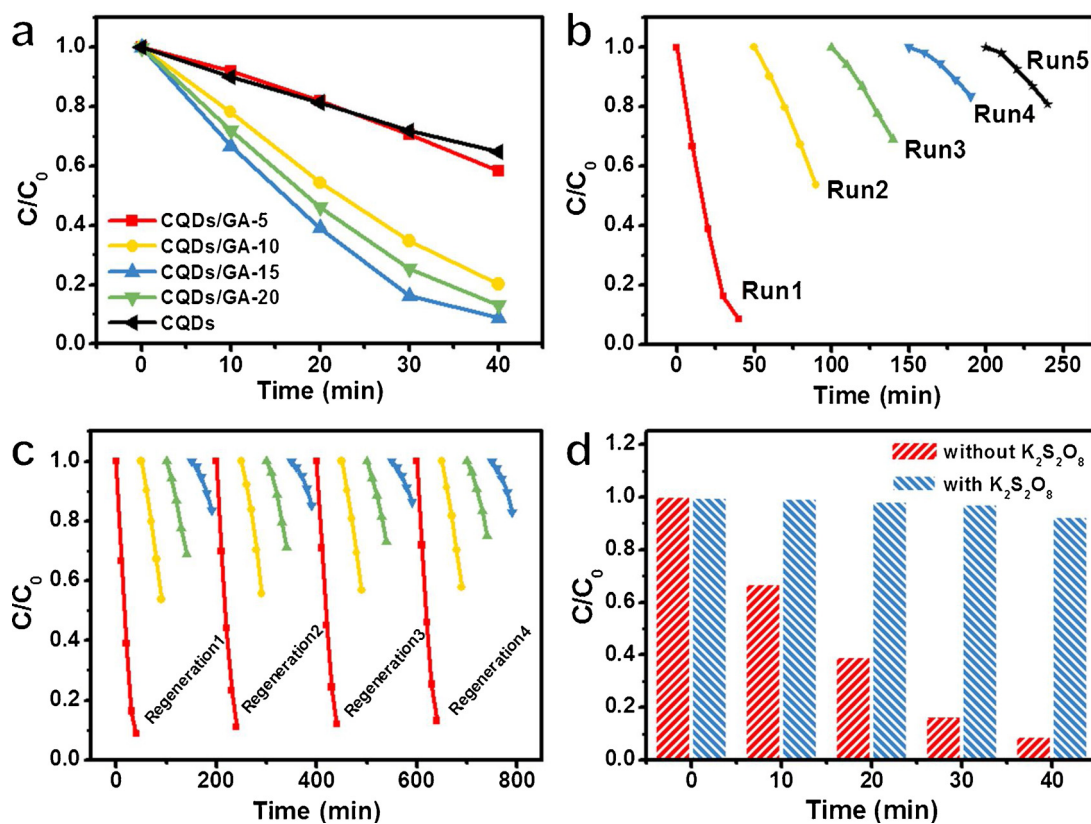


Fig. 4. (a) Photocatalytic reduction of Cr (VI) aqueous solution over the as-prepared CQDs/GA samples, CQDs and GA under UV-vis light irradiation. (b) Recycling test of the CQDs/GA-15 for photocatalytic reduction of Cr (VI) aqueous solution under UV-vis light irradiation. (c) Regeneration test of the CQDs/GA-15 for photocatalytic reduction of Cr (VI) aqueous solution under UV-vis light irradiation. (d) Controlled experiment over the CQDs/GA-15 with and without $K_2S_2O_8$ as a scavenger for photogenerated electrons in photocatalytic reduction of Cr (VI) aqueous solution under UV-vis light irradiation.

(UPS) and UV-vis adsorption spectrum were performed to estimate the valence-band maximum (VBM) of CQDs [34]. As shown in Fig. 3c, the UPS result shows that VBM of CQDs is about 2.01 eV. Based on the VBM and E_g values for direct and indirect transitions of CQDs, if the CQDs undergo an indirect transition, the conduction-band minimum (CBM) value of CQDs is 0.20 eV. However, this CBM potential does not satisfy the thermodynamic potentials for the reduction of Cr (VI) (approximately -0.13 V vs NHE) in alkaline environments ($pH = 8.5$) [35], which suggests that CQDs undergo a direct bandgap transition. Therefore, the CBM value of CQDs is -2.34 eV. Fig. 3d shows the energy band positions of CQDs.

The photocatalytic activity of the CQDs/GA composites was tested by the photoreduction of hexavalent chromium (Cr (VI)) aqueous solution under UV-vis light irradiation, which represents a promising and significant treatment for the detoxification of industrial wastewaters [36,37]. Before UV-vis light irradiation, the reaction system was kept in the dark for 2 h to establish adsorption-desorption equilibrium between the photocatalysts and the reactants. As shown in Fig. S11, the CQDs/GA samples do not display obvious adsorption for Cr (VI). This could be because that the surfaces of CQDs/GA samples are negatively charged (Fig. S12), which repel with CrO_4^{2-} (the mainly existence of Cr (VI) in alkaline solutions [38]). As shown in Fig. 4a, 91.3% of Cr (VI) can be removed over the optimal CQDs/GA-15 within 40 min of UV-vis light irradiation, while only 35.3% of Cr (VI) can be removed over the pristine CQDs. These results suggest that the introduction of GA can distinctly enhance the photocatalytic activity of CQDs. Furthermore, the photocatalytic stability test of the optimal CQDs/GA-15 was conducted as shown in Fig. 4b. The photoactivity of the CQDs/GA-15 decreases to 16.4% during the initial 4 recycle times and keeps nearly unchanged at the 5th recycle time. Considering that stability is as vital as activity for the application of photocatalytic materials, we tried to

regenerate the CQDs/GA composites via a very simple rehydrothermal treatment of the used CQDs/GA photocatalysts with fresh CQDs. As displayed in Fig. 4c, four successive photoactivity tests have proven the photoactivity recovery of the CQDs/GA composites by this simple efficient method.

To gain an insight into the mechanism of the photocatalytic reduction of Cr (VI) over the CQDs/GA composites under UV-vis light irradiation, the controlled experiment with adding $K_2S_2O_8$ as a quenching agent for electrons over the CQDs/GA-15 was performed, as shown in Fig. 4d. It has been observed that the photoreduction of Cr (VI) driven by electrons is distinctly suppressed with the addition of $K_2S_2O_8$ in the reaction system, which indicates the presence of photogenerated electrons over the CQDs/GA-15 under UV-vis light irradiation. Furthermore, the photoelectrochemical (PEC) characterizations of the samples were investigated to understand the origin of the enhanced photocatalytic performance over the CQDs/GA composites [39,40]. Fig. 5a shows transient photocurrent responses of the CQDs/GA-15 and the blank CQDs under intermittent UV-vis light irradiation. The CQDs/GA-15 composite shows obviously enhanced photocurrent responses as compared to the blank CQDs. This result suggests that 3D networks of CQDs/GA can promote the separation of electron-hole pairs generated from the photosensitization of CQDs under UV-vis light irradiation [41]. Fig. 5b features the cyclic voltammograms (CV) of the CQDs/GA-15 and the bare CQDs. Since the preparation of the electrodes and electrolyte are identical for the CV curve measurement, the current density of the electrodes is related to the electron transfer rate of the electrode materials [42]. It has been shown that the current density over the electrodes of the CQDs/GA-15 is larger than that over the blank CQDs, which indicates more efficient separation and transport of photoexcited electron-hole pairs over the CQDs/GA-15 than the pristine CQDs. As displayed in Fig. 5c, the polarization curves of the samples

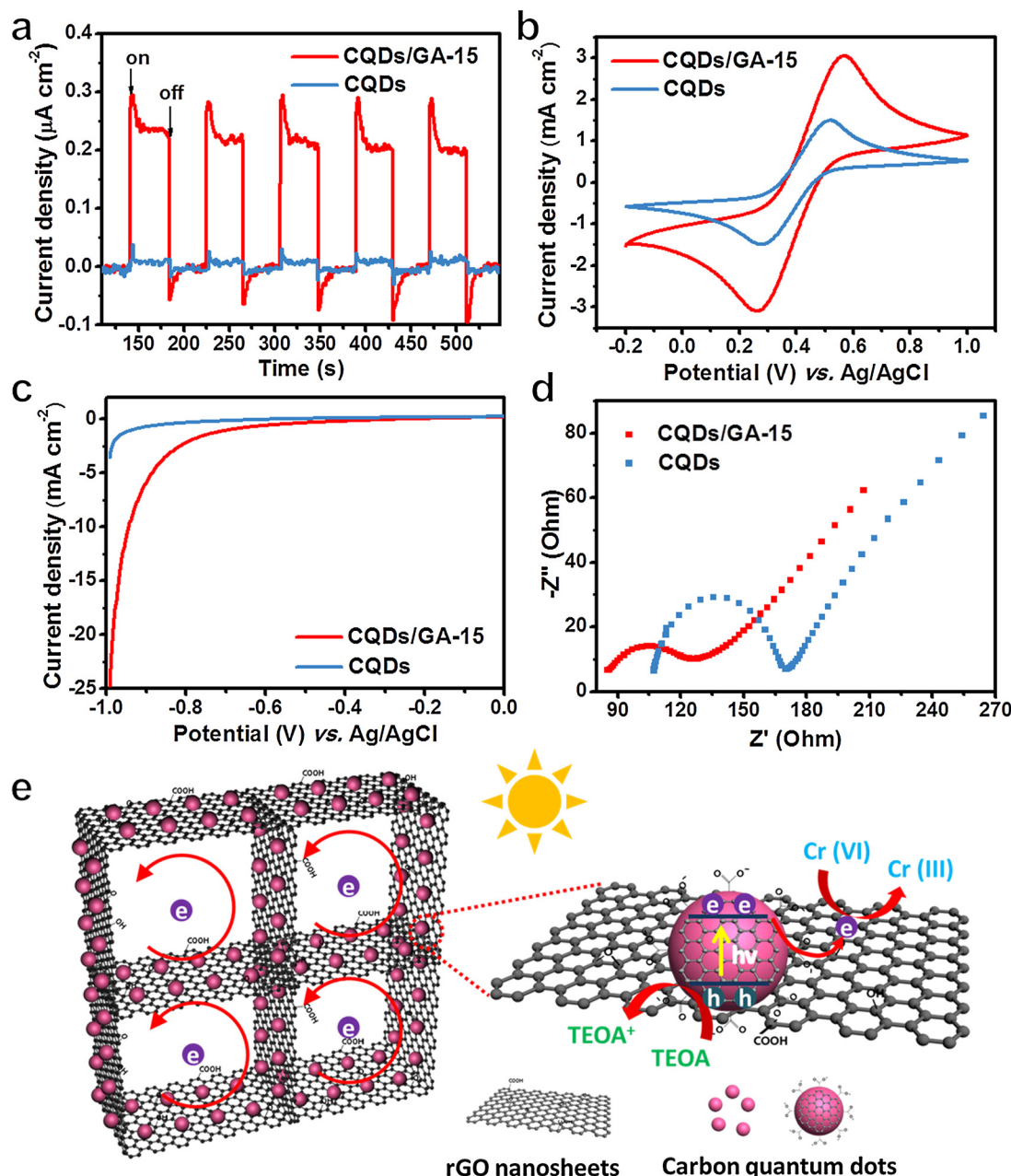


Fig. 5. (a) Transient photocurrent responses of the CQDs/GA-15 and blank CQDs under UV-vis light. (b) Cyclic voltammograms, (c) polarization curves and (d) electrochemical impedance spectroscopy (EIS) of the CQDs/GA-15 and the blank CQDs. (e) Schematic illustration of the proposed reaction mechanism for photocatalytic reduction of Cr (VI) over 3D CQDs/GA photocatalysts.

manifest that the CQDs/GA-15 displays a higher current density at a similar potential range than blank CQDs, implying that the 3D interconnected networks of the CQDs/GA composites can efficiently promote the charge carriers separation and hence contribute to the photoreduction of Cr (VI) [43]. To study the electron transfer process on the electrode and at the contact interface between electrode and electrolyte, the electrochemical impedance spectroscopy (EIS) of the two samples was measured. As shown in Fig. 5d, the Nyquist plot of the CQDs/GA-15 electrode possesses a more depressed semicircle at high frequency, which reveals a more efficient interfacial electron transfer over the electrodes of the CQDs/GA-15 than that of the blank CQDs [44].

On the basis of the above discussions, a possible mechanism for photocatalytic reduction of Cr (VI) over the CQDs/GA composites is illustrated in Fig. 5e. Upon the UV-vis light irradiation, the electrons in

the valence band (VB) are photoexcited to the conduction band (CB) of CQDs in the CQDs/GA composites [33]. The photogenerated electrons subsequently move to the surface of 3D GA through the multi-dimensional electron transfer pathways, which include the 2D graphene nanosheets and the 3D cross-linking frameworks, thereby reducing Cr (VI) to nontoxic Cr (III) [8]. The produced holes are captured by triethanolamine (TEOA), which can further facilitate the separation of photoexcited charge carriers. As a result, the improved separation and transfer of photogenerated electrons significantly contribute to the enhanced performance of the CQDs/GA composites toward photocatalytic reduction of Cr (VI) under ambient conditions.

4. Conclusions

In summary, we have reported a rational design of the CQDs/GA

composites with enhanced photocatalytic performance *via* a facile self-assembly strategy. The comparison characterizations reveal that 3D GA acts as the mediator to boost the extraction and transfer of photo-induced charge carriers from CQDs, thereby leading to the distinctly enhanced activity toward photoreduction of Cr (VI). Moreover, 3D GA can provide benign supports for the immobilization of CQDs, which makes it feasible to recycle the water-soluble CQDs from liquid-phase reaction system. In particular, the CQDs/GA composites can be regenerated *via* a simple rehydrothermal process by supplementing fresh CQDs. This strategy for constructing 3D graphene aerogel frameworks with the merits of low cost, benign conductivity and easy regenerability could inspire the future development of CQD-based composite structures for photoredox applications.

Acknowledgements

The support from the Key Project of National Natural Science Foundation of China (U1463204, 21173045, 20903023 and 20903022), the Award Program for Minjiang Scholar Professorship, the Natural Science Foundation of Fujian Province for Distinguished Young Investigator Rolling Grant (2017J07002), the Independent Research Project of State Key Laboratory of Photocatalysis on Energy and Environment (No. 2014A05), the first Program of Fujian Province for Top Creative Young Talents, and the Program for Returned High-Level Overseas Chinese Scholars of Fujian province is kindly acknowledged.

Appendix A. Supplementary data

Supplementary material related to this article can be found, in the online version, at doi:<https://doi.org/10.1016/j.apcatb.2018.03.108>.

References

- [1] R. Wang, K.-Q. Lu, Z.-R. Tang, Y.-J. Xu, J. Mater. Chem. A 5 (2017) 3717–3734.
- [2] J. Bian, C. Huang, L. Wang, T. Hung, W.A. Daoud, R. Zhang, ACS Appl. Mater. Interfaces 6 (2014) 4883–4890.
- [3] K.A.S. Fernando, S. Sahu, Y. Liu, W.K. Lewis, E.A. Gulians, A. Jafarian, P. Wang, C.E. Bunker, Y.-P. Sun, A.C.S. Appl. Mater. Interfaces 7 (2015) 8363–8376.
- [4] Y.-Q. Zhang, D.-K. Ma, Y.-G. Zhang, W. Chen, S.-M. Huang, Nano Energy 2 (2013) 545–552.
- [5] J. Wang, M. Gao, G.W. Ho, J. Mater. Chem. A 2 (2014) 5703–5709.
- [6] L. Cao, S. Sahu, P. Anilkumar, C.E. Bunker, J. Xu, K.A.S. Fernando, P. Wang, E.A. Gulians, K.N. Tackett, Y.-P. Sun, J. Am. Chem. Soc. 133 (2011) 4754–4757.
- [7] S. Zhuo, M. Shao, S.-T. Lee, ACS Nano 6 (2012) 1059–1064.
- [8] Y. Fan, W. Ma, D. Han, S. Gan, X. Dong, L. Niu, Adv. Mater. 27 (2015) 3767–3773.
- [9] B. Qiu, M. Xing, J. Zhang, J. Am. Chem. Soc. 136 (2014) 5852–5855.
- [10] Z. Tong, D. Yang, J. Shi, Y. Nan, Y. Sun, Z. Jiang, A.C.S. Appl. Mater. Interfaces 7 (2015) 25693–25701.
- [11] Y. Lu, B. Ma, Y. Yang, E. Huang, Z. Ge, T. Zhang, S. Zhang, L. Li, N. Guan, Y. Ma, Y. Chen, Nano Res. 10 (2017) 1662–1672.
- [12] C. Cui, S. Li, Y. Qiu, H. Hu, X. Li, C. Li, J. Gao, W. Tang, Appl. Catal. B 200 (2017) 666–672.
- [13] M.-Q. Yang, N. Zhang, Y. Wang, Y.-J. Xu, J. Catal. 346 (2017) 21–29.
- [14] B. Wang, L. Si, J. Geng, Y. Su, Y. Li, X. Yan, L. Chen, Appl. Catal. B 204 (2017) 316–323.
- [15] Z.-S. Wu, S. Yang, Y. Sun, K. Parvez, X. Feng, K. Müllen, J. Am. Chem. Soc. 134 (2012) 9082–9085.
- [16] K.-Q. Lu, X. Xin, N. Zhang, Z.-R. Tang, Y.-J. Xu, J. Mater. Chem. A 6 (2018) 4590–4604.
- [17] B.C.M. Martindale, G.A.M. Hutton, C.A. Caputo, E. Reisner, J. Am. Chem. Soc. 137 (2015) 6018–6025.
- [18] K.-Q. Lu, N. Zhang, C. Han, F. Li, Z. Chen, Y.-J. Xu, J. Phys. Chem. C 120 (2016) 27091–27103.
- [19] N. Zhang, M.-Q. Yang, Z.-R. Tang, Y.-J. Xu, ACS Nano 8 (2013) 623–633.
- [20] P. He, J. Sun, S. Tian, S. Yang, S. Ding, G. Ding, X. Xie, M. Jiang, Chem. Mater. 27 (2015) 218–226.
- [21] Y. Xu, K. Sheng, C. Li, G. Shi, ACS Nano 4 (2010) 4324–4330.
- [22] W. Lv, C. Zhang, Z. Li, Q.-H. Yang, J. Phys. Chem. Lett. 6 (2015) 658–668.
- [23] H. Li, Z. Kang, Y. Liu, S.-T. Lee, J. Mater. Chem. 22 (2012) 24230–24253.
- [24] S.Y. Lim, W. Shen, Z. Gao, Chem. Soc. Rev. 44 (2015) 362–381.
- [25] S. Ghosh, A.M. Chizik, N. Karedla, M.O. Dekaluk, I. Gregor, H. Schuhmann, M. Seibt, K. Bodensiek, I.A.T. Schaap, O. Schulz, A.P. Demchenko, J. Enderlein, A.I. Chizik, Nano Lett. 14 (2014) 5656–5661.
- [26] L.L. Zhang, X. Zhao, M.D. Stoller, Y. Zhu, H. Ji, S. Murali, Y. Wu, S. Perales, B. Clevenger, R.S. Ruoff, Nano Lett. 12 (2012) 1806–1812.
- [27] R. Zhang, Y. Cao, P. Li, X. Zang, P. Sun, K. Wang, M. Zhong, J. Wei, D. Wu, F. Kang, H. Zhu, Nano Res. 7 (2014) 1477–1487.
- [28] J. Zhou, C. Booker, R. Li, X. Zhou, T.-K. Sham, X. Sun, Z. Ding, J. Am. Chem. Soc. 129 (2007) 744–745.
- [29] X. Li, M. Rui, J. Song, Z. Shen, H. Zeng, Adv. Funct. Mater. 25 (2015) 4929–4947.
- [30] X. Zhao, M. Li, H. Dong, Y. Liu, H. Hu, Y. Cai, Y. Liang, Y. Xiao, M. Zheng, ChemSusChem 10 (2017) 2626–2634.
- [31] D.R. Dreyer, S. Park, C.W. Bielawski, R.S. Ruoff, Chem. Soc. Rev. 39 (2010) 228–240.
- [32] Y. Park, J. Yoo, B. Lim, W. Kwon, S.-W. Rhee, J. Mater. Chem. A 4 (2016) 11582–11603.
- [33] P. Yang, J. Zhao, J. Wang, B. Cao, L. Li, Z. Zhu, J. Mater. Chem. A 3 (2015) 8256–8259.
- [34] M.-L. Yang, N. Zhang, K.-Q. Lu, Y.-J. Xu, Langmuir 33 (2017) 3161–3169.
- [35] Y. Ku, I.-L. Jung, Water Res. 35 (2001) 135–142.
- [36] G. Dong, L. Zhang, J. Phys. Chem. C 117 (2013) 4062–4068.
- [37] N. Wu, H. Wei, L. Zhang, Environ. Sci. Technol. 46 (2012) 419–425.
- [38] C.M. Welch, O. Nekrassova, R.G. Compton, Talanta 65 (2005) 74–80.
- [39] J. Di, J. Xia, M. Ji, B. Wang, S. Yin, Q. Zhang, Z. Chen, H. Li, A.C.S. Appl. Mater. Interfaces 7 (2015) 20111–20123.
- [40] N. Zhang, S. Xie, B. Weng, Y.-J. Xu, J. Mater. Chem. A 4 (2016) 18804–18814.
- [41] C. Han, Q. Quan, H.M. Chen, Y. Sun, Y.-J. Xu, Small 13 (2017) 1602947.
- [42] B. Weng, Q. Quan, Y.-J. Xu, J. Mater. Chem. A 4 (2016) 18366–18377.
- [43] F.-X. Xiao, J. Miao, B. Liu, J. Am. Chem. Soc. 136 (2014) 1559–1569.
- [44] C. Han, Z. Chen, N. Zhang, J.C. Colmenares, Y.-J. Xu, Adv. Funct. Mater. 25 (2015) 221–229.